Experimental Validation of the Quadratic Constitutive Relation in Supersonic Streamwise Corner Flows

Kshitij Sabnis* and Holger Babinsky†
Department of Engineering, University of Cambridge, Cambridge, CB2 1PZ, UK

Daniel S. Galbraith‡ and John A. Benek§
Air Force Research Laboratory, Wright–Patterson AFB, Ohio, United States

The quadratic constitutive relation is a simple extension to the linear eddy-viscosity hypothesis and has shown some promise in improving the computation of flow along streamwise corner geometries. In order to further investigate these improvements, the quadratic model is validated by comparing RANS simulations of a Mach 2.5 wind tunnel flow with high-quality experimental velocity data. Careful set up and assessment of computations using detailed characterisation data of the overall flow field suggests a minimum expected discrepancy of approximately 3% for any experimental–computational velocity comparisons. The corner regions of the rectangular cross-section wind tunnel exhibit velocity differences of 7% between experimental data and computations with linear eddy-viscosity models, but these discrepancies are reduced to 4–5% when the quadratic constitutive relation is used. This improvement can be attributed to a better prediction of the corner boundary-layer structure, due to computations reproducing the stress-induced streamwise vortices which are known to exist in this flow field. However, the strength and position of these vortices do not correspond exactly with those in the measured flow. A further observation from this study is the appearance of additional, non-physical vortices when the value of the quadratic coefficient in the relation exceeds the recommended value of 0.3.

I. Introduction

Streamwise corner flows are often encountered in high-speed flows. For example, the intakes of supersonic aircraft, wing–body junctions, and turbine blade–hub junctions all contain streamwise corners, along which a boundary layer develops. However this geometry, which is often unavoidable, is also problematic. Since the corner region corresponds to the intersection of two viscous boundary layers, it contains very low momentum flow. An adverse pressure gradient, such as due to the impingement of a shock wave, often causes the corner boundary layer to separate. The corresponding stagnation pressure losses can have a significant detrimental effect. For instance, corner effects in the wing-body junction are estimated to contribute 4–6% of the total aircraft drag, while the inlet corner flows are believed to reduce the range of fighter aircraft by 9% [1].

Despite the significance of the corner regions in predicting the wider flow field, corner flows are generally not computed accurately by the Reynolds-averaged Navier–Stokes (RANS) methods typically used in industry. This is largely due to the inability of such computations to capture streamwise vortices in the corner boundary layer, which are known to affect the local flow momentum [2]. These vortices are produced by anisotropies in the Reynolds stresses in the flow, represented by terms A and B in the mean streamwise vorticity equation [3]:

$$\underbrace{v\frac{\partial \omega_x}{\partial y} + w\frac{\partial \omega_x}{\partial z}}_{\text{advection}} = \underbrace{\omega_y\frac{\partial u}{\partial y} + \omega_z\frac{\partial u}{\partial z}}_{\text{vortex-line bending}} + \underbrace{\nu\left(\frac{\partial^2}{\partial y^2} + \frac{\partial^2}{\partial z^2}\right)\omega_x}_{\text{viscous diffusion}} + \underbrace{\left(\frac{\partial^2}{\partial y^2} - \frac{\partial^2}{\partial z^2}\right)\left(-\overline{v'w'}\right)}_{\text{A}} + \underbrace{\frac{\partial^2}{\partial y \partial z}\left(\overline{v'^2} - \overline{w'^2}\right)}_{\text{B}} . \tag{1}$$

In this equation, ω_x, ω_y and ω_z are the vorticity components in the streamwise, wall-normal and spanwise directions, while ν is the kinematic viscosity of the flow.

*Research Associate, Department of Engineering, University of Cambridge.
†Professor in Aerodynamics, Department of Engineering, University of Cambridge, AIAA Fellow.
‡Engineer, Computational Sciences Centre, AFRL Aerospace Systems Directorate.
§Director, Computational Sciences Centre, AFRL Aerospace Systems Directorate, AIAA Fellow.

The difficulty faced by RANS computations in capturing the vortices is thought to be related to the reliance of popular turbulence models on the linear eddy-viscosity hypothesis, which has remained popular due to its simplicity and low computational cost, as compared to more involved closure models. Linear eddy-viscosity models (LEVMs) estimate the Reynolds stress tensor, $\tau_{ij} = -\rho\overline{u_i' u_j'}$, using the Boussinesq assumption:

$$\tilde{\tau}_{ij} = 2\mu_t S^*_{ij} + \frac{2}{3}\rho k \delta_{ij} \ , \tag{2}$$

where $\tilde{\tau}_{ij}$ is the estimated Reynolds stress tensor and μ_t is the eddy viscosity. In this equation, the traceless stress tensor $S^*_{ij} = S_{ij} - 1/3\frac{\partial u_k}{\partial x_k}\delta_{ij}$, with δ_{ij} denoting the Kronecker delta, and $S_{ij} = 1/2\left(\frac{\partial u_i}{\partial x_j} + \frac{\partial u_j}{\partial x_i}\right)$. The density is given by ρ and k corresponds to the turbulent kinetic energy. Note that the second term, $2/3\rho k\delta_{ij}$, is neglected in one-equation turbulence models, which have instead:

$$\tilde{\tau}_{ij} = 2\mu_t S^*_{ij} \ . \tag{3}$$

Equations 2 and 3 both produce a simple distribution of turbulent stresses. In particular, $\overline{v'v'} = \overline{w'w'}$ and $\overline{v'w'} = 0$, and so the vorticity production terms (A and B in Eq. 1) both evaluate to zero. As a result, RANS simulations based on linear eddy-viscosity models are unable to generate the streamwise vortices which exist in corner boundary layers, resulting in a poor prediction of these flows.

One approach to extend the capabilities of LEVMs with only a mild increase in complexity is to consider terms that are quadratic in the mean vorticity and strain tensors, when evaluating the Reynolds stress tensor. These extensions to the Boussinesq assumption still relate the eddy viscosity with the turbulent stresses using only properties of the mean flow, rather than any variables specific to the turbulence model in use. There have been two iterations of the quadratic constitutive relation (QCR), developed by Spalart. The original statement of the relation, QCR-2000 [4], applies a modification to the Boussinesq assumption, and is defined by:

$$\tilde{\tau}_{ij} = 2\mu_t S^*_{ij} - \frac{4c_{cr1}\mu_t}{\sqrt{S_{kl}S_{kl} + \Omega_{kl}\Omega_{kl}}}\left[\Omega_{ik}S^*_{kj} - S^*_{ik}\Omega_{kj}\right] \ , \tag{4}$$

where the strain tensor $\Omega_{ij} = 1/2\left(\frac{\partial u_i}{\partial x_j} - \frac{\partial u_j}{\partial x_i}\right)$. Note that since this modification uses only mean-flow properties, it can be applied to any single-equation or multi-equation turbulence model that is based on a linear eddy-viscosity model. The additional term $2/3\rho k\delta_{ij}$ can be included for turbulence models which provide the turbulent kinetic energy, k.

A more recent version of this relation, QCR-2013 [5], was proposed for one-equation turbulence models which do not provide k and includes an additional term:

$$\tilde{\tau}_{ij} = 2\mu_t S^*_{ij} - \frac{4c_{cr1}\mu_t}{\sqrt{S_{kl}S_{kl} + \Omega_{kl}\Omega_{kl}}}\left[\Omega_{ik}S^*_{kj} - S^*_{ik}\Omega_{kj}\right] - c_{cr2}\mu_t\left[\sqrt{2S^*_{kl}S^*_{kl}}\right]\delta_{ij} \ . \tag{5}$$

This additional term $c_{cr2}\mu_t\left[\sqrt{2S^*_{kl}S^*_{kl}}\right]\delta_{ij}$ approximately accounts for the $2/3\rho k\delta_{ij}$ term in the Boussinesq equation (Eq. 2), which had been omitted in Eqs. 3 and 4. The constants c_{cr1} and c_{cr2} were proposed as 0.3 and 2.5, respectively, after calibration in the outer part of an equilibrium turbulent boundary layer [5].

A recent version of the model, termed QCR-2020, has been proposed by Rumsey *et al.* [6]. In this formulation, the constants, c_{cr1} and c_{cr2}, are no longer assumed to be spatially uniform but are replaced with equivalent coefficients containing wall-normal dependency, which vary from one value at the walls to a different one near the boundary-layer edge. Given the relative infancy of the QCR-2020 extension and its inherent added complexity, this paper instead focuses on QCR-2013, which has constant coefficient values and whose implementation in RANS solvers is well-established [7–10].

All formulations of QCR have appeared to demonstrate some success in corner flow prediction. Rumsey *et al.* found that the estimate of corner separation is improved by QCR [10], and Dandois *et al.* demonstrated that these improvements extend to shock-induced separation in transonic and supersonic flows [7]. These studies compare the size and shape of the corner separation extracted from computations against experiment. However, the velocity distribution within corner boundary layer itself has not been measured experimentally. It is therefore not possible to fully understand why QCR has improved prediction of corner separation, or to evaluate the extent of the model's capabilities. One plausible explanation is that computations using QCR are able to generate streamwise vortices within the corner boundary layer [5, 9], which had not been captured by LEVMs, but this hypothesis can not be confirmed using existing data sets. In addition, the extent to which the properties of the vortices in these RANS simulations (position, strength, etc.) coincide

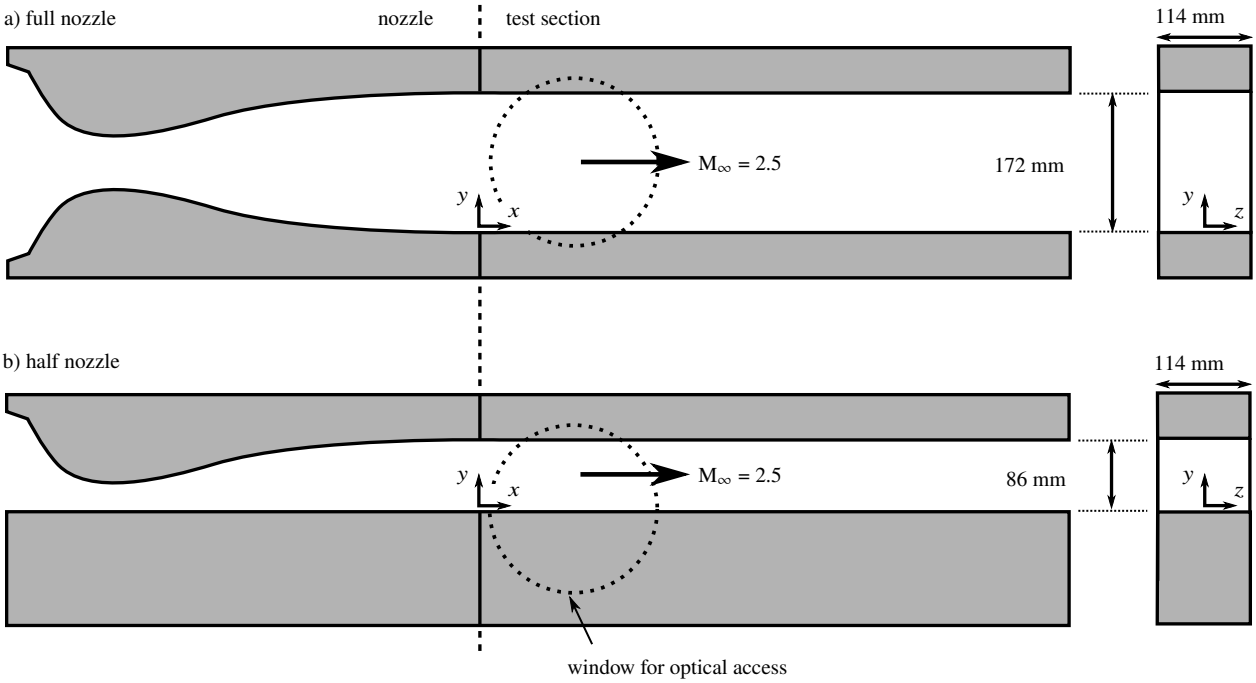

Fig. 1 Wind tunnel setup for a) the full and b) the half nozzle configurations. The dashed circle corresponds to a window in the tunnel sidewall, which provides optical access.

with those of the physical flow remains yet to be established. This paper therefore aims to address the resulting gap in knowledge by evaluating the capabilities and limitations of QCR using supersonic corner flow data obtained from wind tunnel experiments.

II. Wind tunnel experiments

A. Experimental methodology

Experiments are performed in Supersonic Wind Tunnel No. 1 at Cambridge University Engineering Department. This is a blow-down wind tunnel, driven by a high-pressure reservoir. The nominal freestream Mach number is fixed at $M_\infty = 2.5$ for this study. The corner boundary layers of supersonic wind tunnels are known to be strongly influenced by the nozzle geometry. Therefore, in order to investigate two distinct corner flow topologies, the tunnel is operated in both a full and half nozzle configuration, as depicted in Fig. 1.

An empty wind tunnel configuration is used in this study, and the measurements focus on the turbulent, naturally-grown boundary-layers on the tunnel surfaces. The rectangular working section of the tunnel has a width of 114 mm, and a height of 172 mm and 86 mm for the full and half configurations respectively. The coordinate system convention is shown in Fig. 1: x represents the streamwise direction, as measured from the end of the nozzle; y indicates the floor-normal direction, with $y = 0$ mm set at the tunnel floor; z is the spanwise coordinate measured from the centre span, such that $z = \pm 57$ mm correspond to the tunnel sidewalls.

The stagnation pressure is set to 308 ± 1 kPa and the operating stagnation temperature is measured as 285 ± 5 K; this corresponds to a nominal unit Reynolds number of 31×10^6 m^{-1}. Within the optically accessible region of the working section (60–120 mm downstream of the nozzle exit), the tunnel boundary-layers are approximately 7 mm to 8 mm thick. They therefore have a Reynolds number based on incompressible displacement thickness of around $\mathrm{Re}_{\delta_i^*} = 30,000$.

Several experimental techniques are used to probe the flow. A z-type schlieren system with a horizontal knife-edge enables visualisation of spanwise-averaged density gradients associated with flow features in the working section. Steady-state surface pressure measurements are performed using static pressure taps with 0.3 mm diameter. The taps are located across the tunnel sidewall, allowing the pressure distributions over this surface to be measured to an accuracy of $\pm 1\%$.

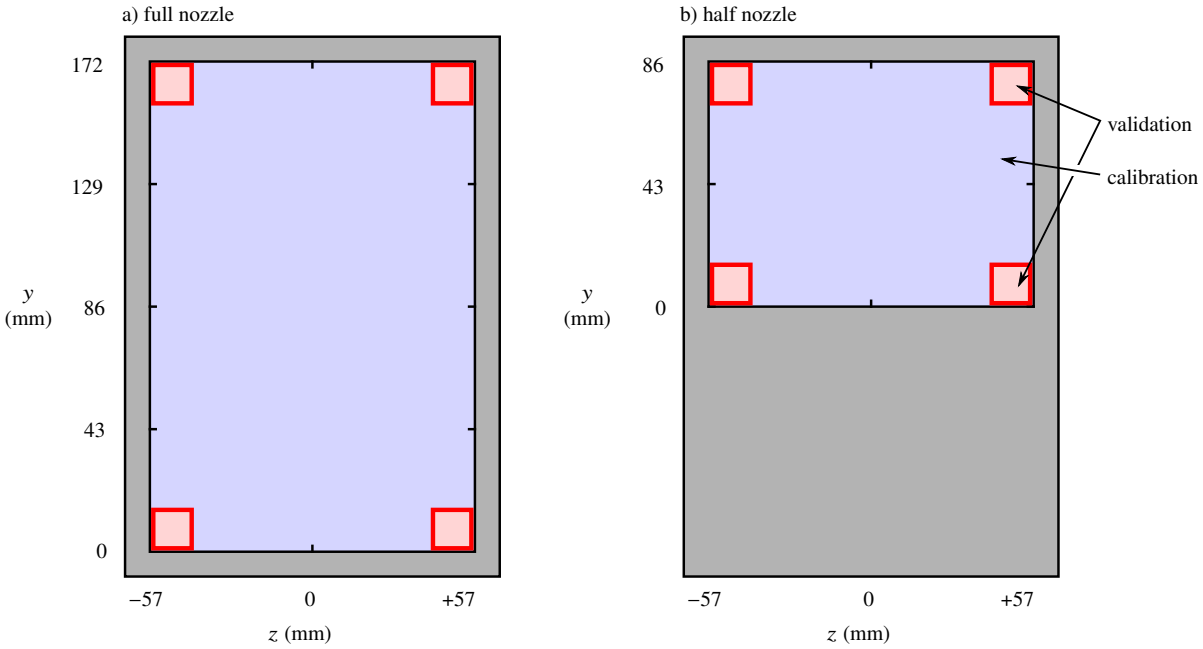

Fig. 2 Division of regions for the purpose of validation (red) and of flow characterisation i.e. the set up of computations (blue) for a) the full nozzle setup, and b) the half nozzle setup.

The streamwise flow velocity, u, is measured by laser Doppler velocimetry (LDV). The flow is seeded with paraffin in the settling chamber. Previous measurements in this facility of particle lag through a normal shock have placed the seeding droplet diameter in the range $200 - 500$ nm [11]. The measured velocities have an error of 2%, due to the finite number density of seeding particles and due to the laser optics. In practice, laser Doppler velocimetry is not precisely a point-measurement technique, since velocities are averaged over a nominal ellipsoidal probe volume which spans 0.1 mm in the streamwise and vertical directions, and 2 mm in the spanwise direction. The positional accuracy of this probe volume is, approximately, $\Delta x \approx 0.2$ mm, $\Delta y \approx 0.005$ mm, and $\Delta z \approx 0.1$ mm.

Boundary-layer traverses are carried out with a spatial resolution of around 0.1 mm. The measured velocity data is then fitted to theoretical profiles. A Sun & Childs (1973) fit [12], adapted to include a van Driest compressibility correction, is used for the outer layer; this combines a log-law of the wall region with a Coles wake function. The viscous sublayer is modelled using a Musker (1979) fit [13]. These fitted profiles are then used to calculate characteristic boundary-layer integral parameters. This avoids errors caused by poor measurement resolution near the wall and therefore provides a more accurate estimate of integral boundary-layer parameters. The boundary-layer properties are determined in their incompressible forms, as these are less sensitive to variations in Mach number and require fewer assumptions to calculate from raw velocity data. The LDV data obtained in this study typically has around 40 measurement points within the boundary layer and the closest data point to the wall is at around $y^+ = 80$. This corresponds to an uncertainty in integral parameters of around 5% for an equilibrium turbulent boundary layer [14].

B. Characterisation of flow quality

In order to ensure that the computations are not tuned using experimental validation data, separate regions are designated for flow characterisation and for validation purposes. Figure 2 shows that the validation region is restricted to the 15 mm × 15 mm region around each wind tunnel corner, whilst the remainder of the flow field is used to characterise the quality of the flow and to set up computations.

Schlieren images are captured for both nozzle configurations used in the current study. Figures 3a and 3b show that the flow in the tunnel is established. It is also possible to identify the boundary layers along the tunnel's floor and ceiling, as well as waves emanating from imperfections in these surfaces.

The strength of the waves identified in Fig. 3 is quantified using steady-state surface pressure measurements on the tunnel sidewall. For the full nozzle setup, Fig. 4a shows that the wall static pressure varies by 4% throughout the working section. These deviations correspond to departures in Mach number of 0.02 from a mean value of 2.48. The

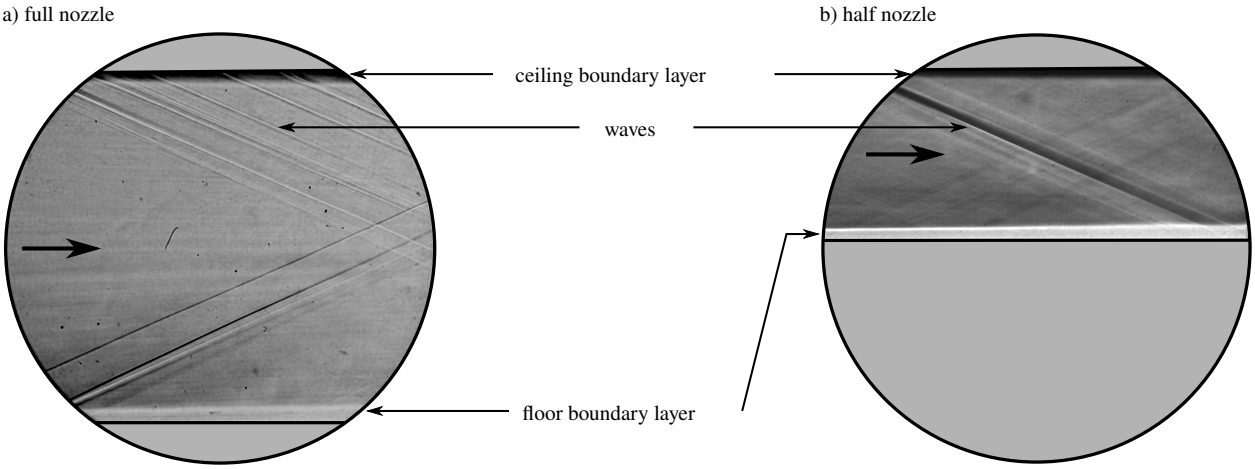

Fig. 3 Schlieren image for the empty tunnel with flow established for a) the full nozzle setup, and b) the half nozzle setup.

oblique features in the plots correspond to weak waves generated from the tunnel floor and ceiling. The wave angle is approximately $24 \pm 2^\circ$ which, for a Mach 2.5 flow, matches closely to the Mach angle (23.6°). These waves can therefore be treated as isentropic. Meanwhile, the vertical columns are likely due to spanwise-travelling waves generated at the sidewalls. The angle of these waves can not be extracted from the data in Fig. 4a. However, the fact that the Mach number varies by less than 1% in the test section does imply that these waves are also weak.

The equivalent data for the half nozzle configuration is presented in Fig. 4b. Here, the static pressure variation across the test section is approximately 7%. The wall pressures correspond to a mean Mach number of 2.44, and associated deviations from this value of 0.03. As for the full nozzle, the pressure distribution exhibits both oblique and vertical features. These correspond to waves generated by imperfections in the tunnel floor and ceiling (oblique), and in the sidewalls (vertical). A comparison of the static pressures and the schlieren images indicates that these waves are stronger than for the full setup, though they are still weak in nature.

Velocity data is obtained for the boundary layer away from the symmetry plane, and on the sidewalls. The measured velocity distribution is shown in Fig. 5, for the two nozzle configurations. The core flow represents a large fraction of the channel area for both setups. The floor and ceiling boundary-layers have approximately constant thickness across the tunnel span, but there is a significant variation in sidewall boundary-layer thickness. This variation can be attributed to known secondary flows which are induced by vertical pressure gradients within the nozzle region. These secondary flows take the form of vertical velocities within the sidewall boundary layers, directed from the corners towards the tunnel centre height in the full nozzle setup and from the top to the bottom corners for the half nozzle [15].

C. Corner flow validation data

The two nozzle geometries studied in this paper are known to produce quite distinct corner flows [15]. The streamwise velocity component in the 15 mm $\times$ 15 mm regions around each corner of the channel is measured at $x = 120$ mm. This velocity distribution is shown for the full nozzle setup in Fig. 6a and for the half nozzle setup in Fig. 6b. There appear to be two distinct flow topologies. All four corners of the full nozzle setup and the top corners of the half nozzle configuration are similar in nature. Meanwhile, the bottom corners with the half nozzle have a thicker sidewall boundary-layer and, therefore, lower-momentum flow in this region.

The secondary flows which influence the sidewall boundary-layer thickness distribution in Fig. 5 are thought to strongly influence the corner regions. These vertical velocity components within the sidewall boundary layers are indicated in Fig. 6 by solid arrows.

Firstly, the secondary flows affect the thickness of the corner boundary layers. Note that the floor/ceiling boundary-layer thickness is approximately the same for all flows shown in Fig. 6, which suggests that the differences in the corner boundary layer depend primarily on the thickness of the constituent sidewall boundary layer. This property is, in turn, directly determined by the sidewall secondary flows. All corners in the full nozzle setup and the bottom corners of the half nozzle setup have the sidewall secondary flow directed vertically away from the corner. This bulk flow

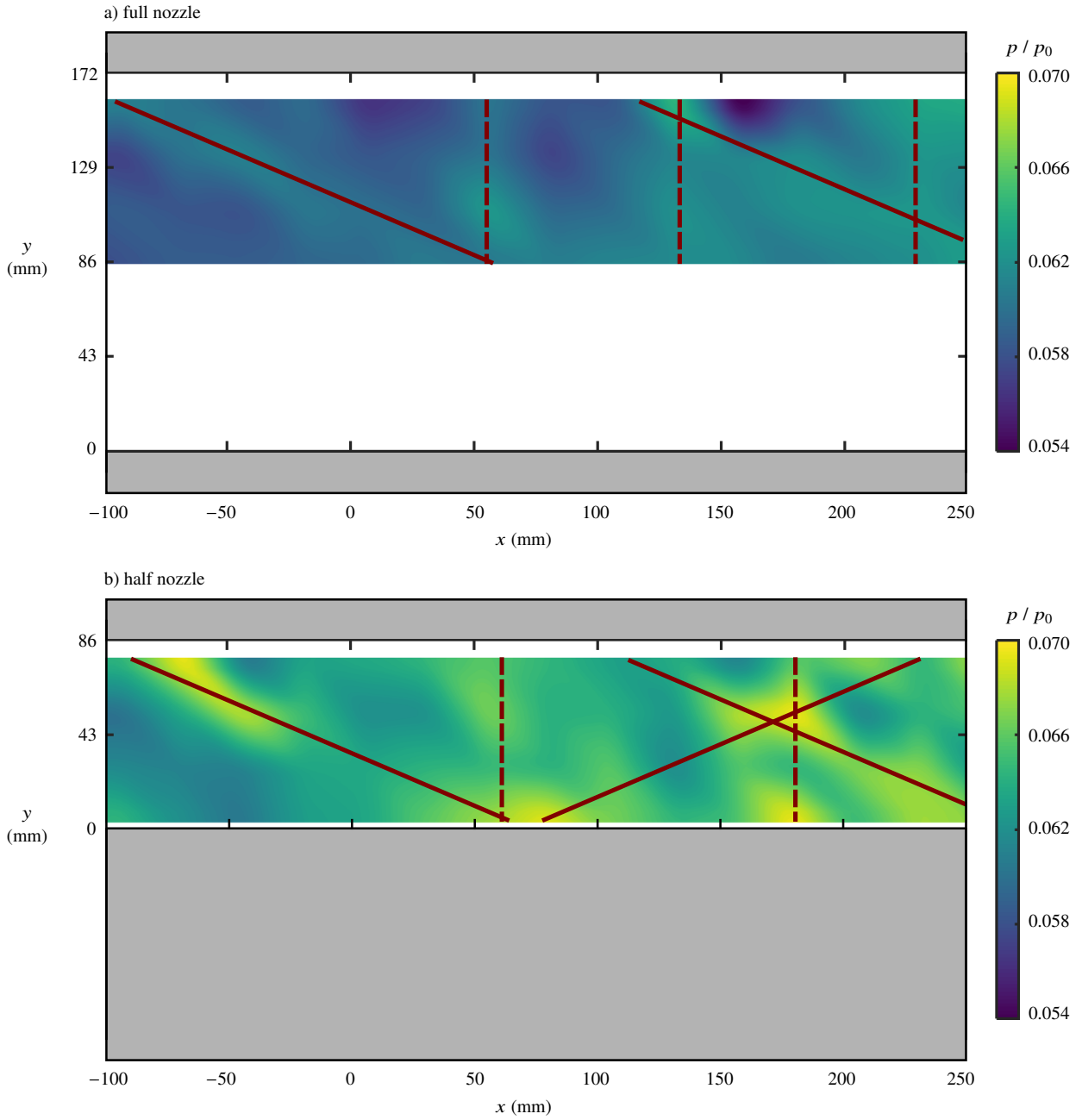

Fig. 4 Static pressure distribution measured using taps located in the tunnel sidewall for a) the full nozzle setup, and b) the half nozzle setup. The red lines correspond to high-pressure areas, which take the form of oblique (solid) and vertical (dashed) regions.

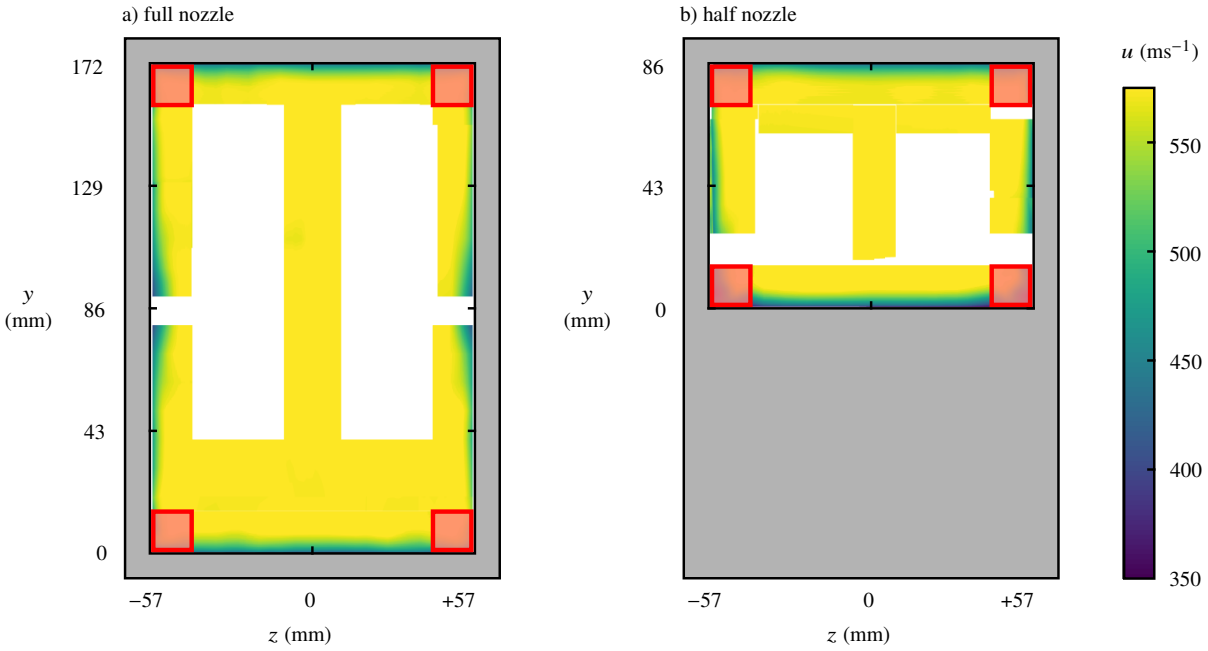

Fig. 5 Streamwise flow velocities measured across the tunnel cross-section at $x = 120$ mm. Corner regions, marked by red boxes, are excluded for characterisation purposes. Regions with an insufficient number density of seeding particles for high-quality velocity measurements are in white.

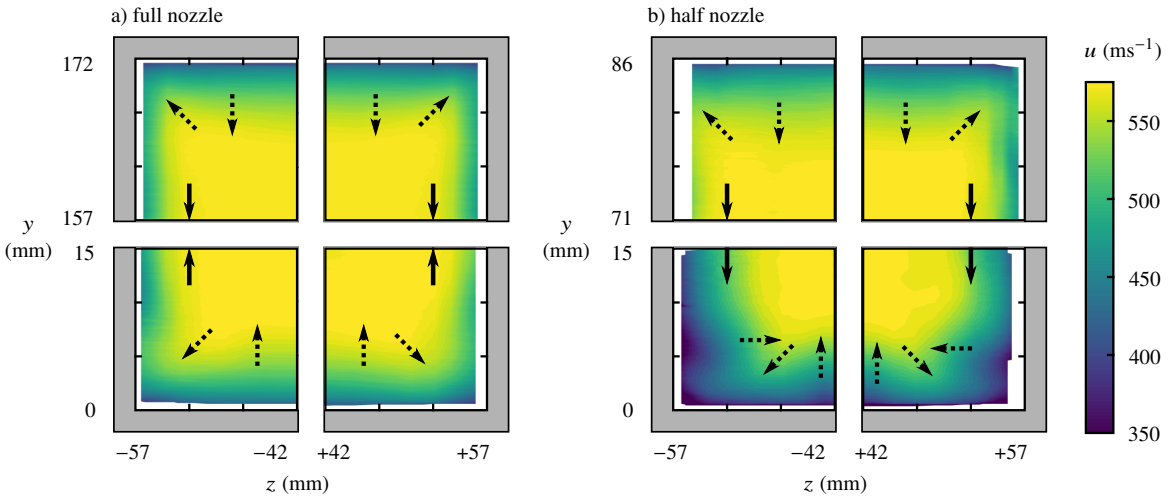

Fig. 6 The streamwise velocity (u) in 15 mm × 15 mm regions around all four tunnel corners for a) the full nozzle setup, and b) the half nozzle setup. These are measured at x = 120 mm. Solid arrows indicate the direction of sidewall secondary flows, and dashed arrows indicate local regions of momentum transfer.

transports the low-momentum fluid in the sidewall and corner boundary layers away from the region. As a result, in the vicinity of these corners, the sidewall boundary layers are thin. The bottom corners of the channel in the half nozzle setup are different, however. Here, the sidewall secondary flows are in the downwards direction, and so they advect low-momentum fluid into the corner region. This results in an increase in the thickness of the boundary layer, consistent with the experimental data from Fig. 6b.

Secondly, a closer examination of Fig. 6 reveals that the boundary-layer thickness is not the only defining feature of this flow. In particular, there are some regions where the high momentum core flow persists into the boundary layer and others where low momentum fluid extends locally into the core. Such regions are indicated by dashed arrows which show the approximate location and direction of these momentum transfers. It is thought that these are caused by the streamwise vortices embedded in the viscous corner flow regions.* The momentum transfers in the bottom corners of the half nozzle setup would be consistent with the presence of two counter-rotating vortices, while the other measured corners appear to contain only a single primary vortex residing on the floor or ceiling. These different inferred vortex structures are consistent with the advection of any vortex embedded in the sidewall boundary layer by the nozzle-induced secondary flows [15].

The sidewall secondary flows therefore cause two very different corner flows in the bottom corner regions of the full and half nozzle setups. These are both used as independent validation data sets for direct comparison with RANS simulations.

III. RANS computations

A. Numerical methodology

The experimental data is used to validate RANS simulations of the wind tunnel flow. For this type of validation study, it is essential that the computations faithfully represent the flow in the physical wind tunnel. This is achieved by setting up the simulations using comprehensive flow characterisation data, as detailed in Ref. [16].

The nozzle geometry-dependence of the corner flows requires the computations to have knowledge of the nozzle region, and so the entire tunnel flow is computed from the settling chamber to well downstream of the working section. Only one quarter of the tunnel with the full nozzle is modelled since it is, in theory, top–bottom and left–right symmetric. Similarly, only one half of the tunnel with the half nozzle configuration is simulated.

The Chimera overset grid technique [17] is used to create a smooth mesh in the contraction and at the sharp corner upstream of the nozzle. The final grid system, shown in Fig. 7, is created using the mesh generation software Pointwise [18], contains 181.7M points across seven grids. A viscous wall spacing of 1.5×10^{-7} m is used with a growth rate of 5%; this produces $y^+ < 1$ at the first point from the wall. The solver OVERFLOW 2.2l [19] is used to solve the RANS equations using the third-order accurate upwind finite difference HLLC scheme [20] combined with the Koren limiter [21]. The time integration uses an unfactored SSOR implicit solution algorithm [22].

The validation process compares corner flow measurements against simulations using the Spalart–Allmaras [23, 24], Menter SST [25, 26], and Wilcox k–ω [27, 28] turbulence models. It is important to ensure that any observed differences in the corner regions are not due to any turbulence-model sensitivity of the global flow computation. Therefore, centre-span floor boundary-layer profiles for these turbulence models are compared for the full nozzle setup in Fig. 8a. The minimal differences between the profiles shows that computations of this flow away from the corners appear to be insensitive to the turbulence model used.

To conduct a grid resolution study on the full nozzle setup while maintaining the point distribution of the original grid, every other point is removed to create a medium grid (22.9M points), and every other point is removed from the medium grid to produce a coarse grid (2.9M points). Figure 8b shows the centre-span boundary-layers on the test section floor for the three grid levels. The three velocity profiles are coincident, indicating that the centre-span profiles have reached grid convergence.

B. Assessment of computational accuracy

The accuracy of computations is evaluated using a range of characterisation data, in order to test how well the physical wind tunnel flow is captured. In particular, this is assessed by comparing computational data with the

*Unfortunately, the inherent limitations of a two-component LDV setup prevent direct identification of the the vortices themselves. Instead, it is necessary to infer the vortex topology by considering the regions of momentum transfer between the core flow and the boundary layers. This indirect method requires correct interpretation of the shape of the complex corner boundary layer, and so the inferred vortex topology may be prone to errors. As a result, the following discussion should be treated with some degree of caution.

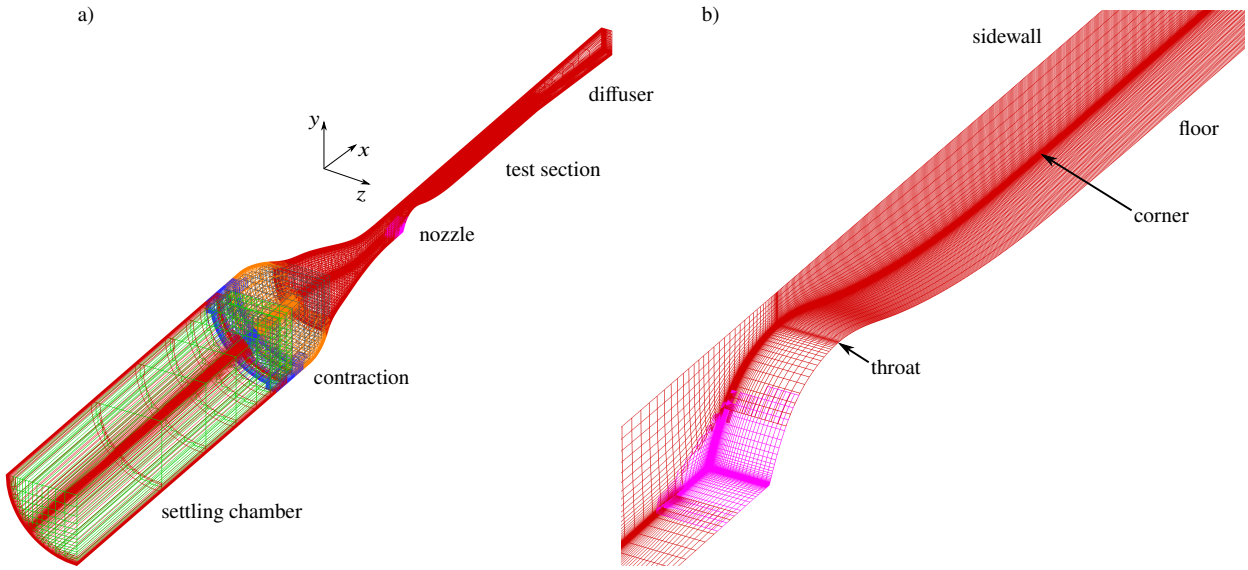

Fig. 7 Representation of mesh used in computations to simulate physical tunnel for the full nozzle setup: a) isometric view of entire mesh; b) surface grid in nozzle and start of test section. One quarter of the wind tunnel is shown.

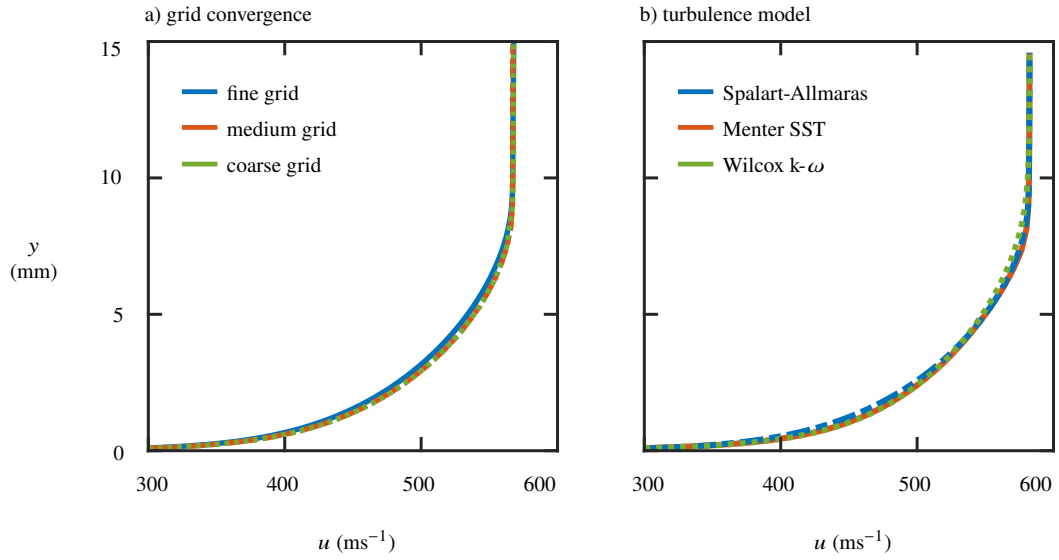

Fig. 8 Floor boundary-layer profiles computed on the centre span at $x = 60$ mm: a) comparison of profiles for the coarse, medium and fine grids; b) comparison of profiles for the Spalart–Allmaras, Menter SST and Wilcox k–ω turbulence models.

experimentally-obtained pressure profile through the test section, the velocities across the channel cross-section, and the profile of the boundary layers growing along the walls. Note that, as illustrated in Fig. 2, this stage of the process excludes the corner regions of the flow field, which are restricted for validation purposes. The assessment of computational accuracy is described in detail in Ref. [16], and the key results are summarised below.

For the full nozzle setup, the difference between the computational (Fig. 9a-i) and experimental (Fig. 4a) sidewall pressure distributions is plotted in Fig. 9a-ii. The difference in the static pressure ratio p/p_0 is around 3×10^{-3}, which corresponds to a Mach number discrepancy of about 1.5%.

The equivalent computational data for the half nozzle setup is given in Fig. 9b-i. The difference compared to the measurements from Fig. 4b are plotted in Fig. 9b-ii. The discrepancy in static pressure ratio is roughly 6×10^{-3}, larger than the equivalent full nozzle comparison. Note, however, that this still corresponds to a relatively small difference in the corresponding Mach number of approximately 2.4%.

In both nozzle setups, the computations appear to under-predict the pressure, with the flow expanding to a lower pressure and a higher Mach number than the experiment. The top-left corner shows a higher pressure region that is just completing its expansion through the nozzle. The simulations appear to capture the weak waves generated by the tunnel floor and ceiling, which indicates that these correspond to uncancelled waves from the nozzle. However, the computations do not seem to reproduce the vertical features, which are believed to be waves from the tunnel sidewalls.

The accuracy of computations is also evaluated by comparing the boundary layer profiles to experiment. This is performed at various streamwise stations for the floor boundary layer on the centre span, assumed to be representative of the boundary layers growing along the wind tunnel walls.

A comparison between computational and experimental floor boundary-layer profiles is presented for the full nozzle in Fig. 10a and for the half nozzle in Fig. 10b. In both cases the freestream velocity and the general profile shape appear to be in good agreement. The profiles do, however, differ slightly at the edge of the boundary layer for both nozzle setups.

A more quantitative assessment of the agreement between computations and experiment is performed by calculating the relevant boundary layer parameters for the profiles in Fig. 10. These are listed in Table 1. There is a good agreement of the integral parameters (δ_i^*, θ_i, and H_i). The deviations from experimental values are generally on the order of 4%. With an experimental uncertainty in these quantities of 5%, the computations do appear to predict these boundary-layer parameters with good accuracy.

Note however, that the deviations from experimental values of the boundary-layer thickness, δ, are on the order of 15%. This parameter therefore does not appear to be predicted particularly well by the computations. Whilst the boundary-layer thickness is known to be less robust than the corresponding integral parameters, the differences are believed to be largely due to the discrepancies in velocity near the boundary-layer edge. These discrepancies, whilst slightly larger than the estimated experimental uncertainties, are relatively minor – the maximum velocity difference is 3%.

A final metric which can be used to evaluate how well the computations capture the physical flow is the streamwise velocity across the tunnel cross-section. The measurements from Fig. 5 are compared to equivalent computational data, which are presented in Figs. 11a-i and 11b-i. These figures appear, on first glance, to be consistent with the experimental data – there is a large core region, the floor/ceiling boundary layers are spanwise-uniform with similar thicknesses, and there are significant variations in the thickness of the sidewall boundary layer. The sidewall boundary layer is thickest at the centre height for the full nozzle setup and at the bottom corners of the half nozzle setup.

A more quantitative measure of agreement can be obtained by calculating the difference between the computed and the experimental velocity distributions. This difference is shown in Figs. 11a-ii and 11b-ii for the two nozzle setups. In these figures, the velocities at most locations differ by no more than 10 ms^{-1}, or 1.7% of the freestream velocity. The notable exception is the sidewall boundary layers, where the discrepancy with experiment can be twice this large. Even though the calculation of the sidewall boundary layers is not fully accurate, 95% of data points have no more than 3.2% error for the full nozzle setup (11a-iii) and 3.5% error for the half nozzle setup (11b-iii).

This level of discrepancy is consistent with the differences between computed and experimental floor boundary-layer profiles, shown in Fig. 10. This is slightly larger than the estimated experimental error, indicating that the computations do not quite compute the true wind tunnel flow. However, a 3.5% error is considered to be small enough to show that the simulations do capture the flow sufficiently well to be used for validation purposes. Moreover, the differences between the two velocity distributions in this relatively well-understood part of the flow field can be used as a baseline 'expected

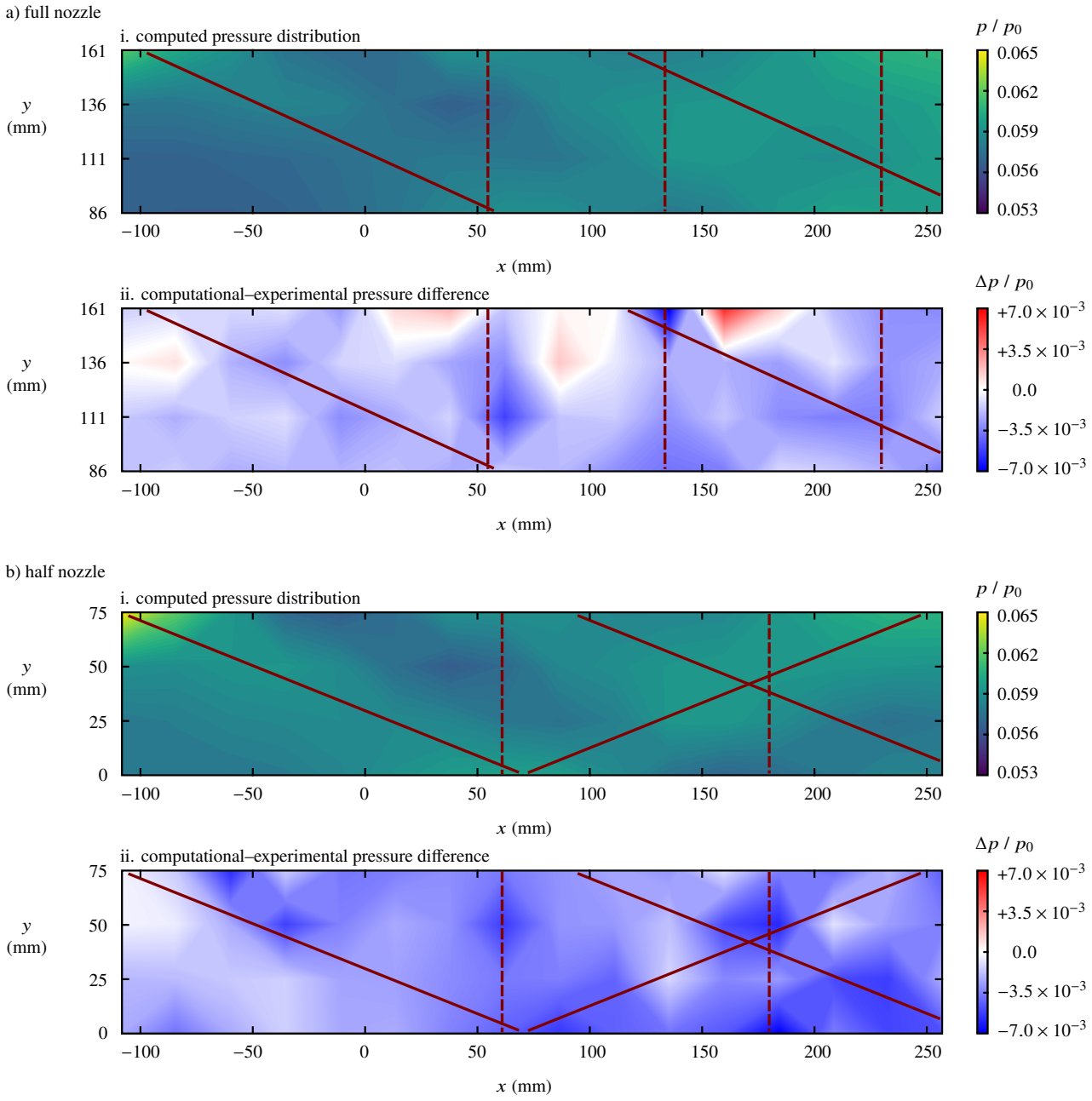

Fig. 9 Static pressure on the tunnel sidewall for a) the full nozzle setup and b) the half nozzle setup: i. the computed pressure distribution, and ii. the difference between the computed pressure distribution and equivalent experimental data (Fig. 4). The red lines correspond to high-pressure areas; these take the form of oblique (solid) and vertical (dashed) regions.

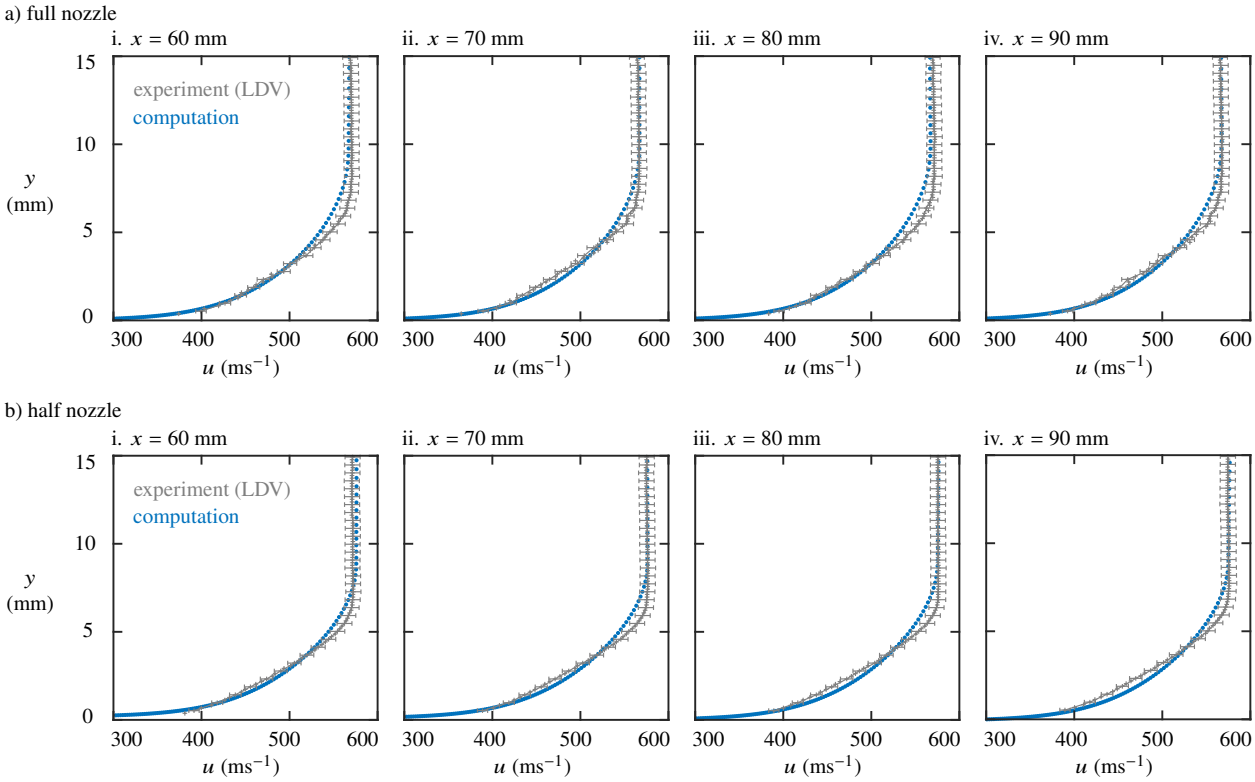

Fig. 10 Comparison between computational and experimental floor boundary-layer profiles, with a) the full nozzle setup, and b) the half nozzle setup. The profiles are shown for the centre span at: i. x = 60 mm, ii. x = 70 mm, iii. x = 80 mm, and iv. x = 90 mm.

Table 1 Incompressible floor boundary-layer parameters, on the tunnel centre span, extracted from the RANS computations. These correspond to CFD profiles presented in Fig. 10a (full nozzle) and Fig. 10b (half nozzle).

	experiment				computation			
x (mm)	δ (mm)	δ_i^* (mm)	θ_i (mm)	H_i	δ (mm)	δ_i^* (mm)	θ_i (mm)	H_i
full nozzle								
60	7.49	0.97	0.73	1.34	8.43	0.96	0.74	1.30
70	7.59	1.03	0.76	1.35	8.49	0.96	0.74	1.29
80	7.70	1.05	0.78	1.36	8.63	0.97	0.75	1.29
90	7.71	1.05	0.78	1.35	8.77	0.99	0.77	1.29
half nozzle								
60	6.80	0.92	0.68	1.36	7.89	0.96	0.73	1.32
70	7.03	0.98	0.72	1.37	8.02	0.96	0.73	1.31
80	7.14	0.99	0.73	1.36	8.38	0.97	0.74	1.30
90	7.26	0.99	0.73	1.36	8.69	0.97	0.75	1.30

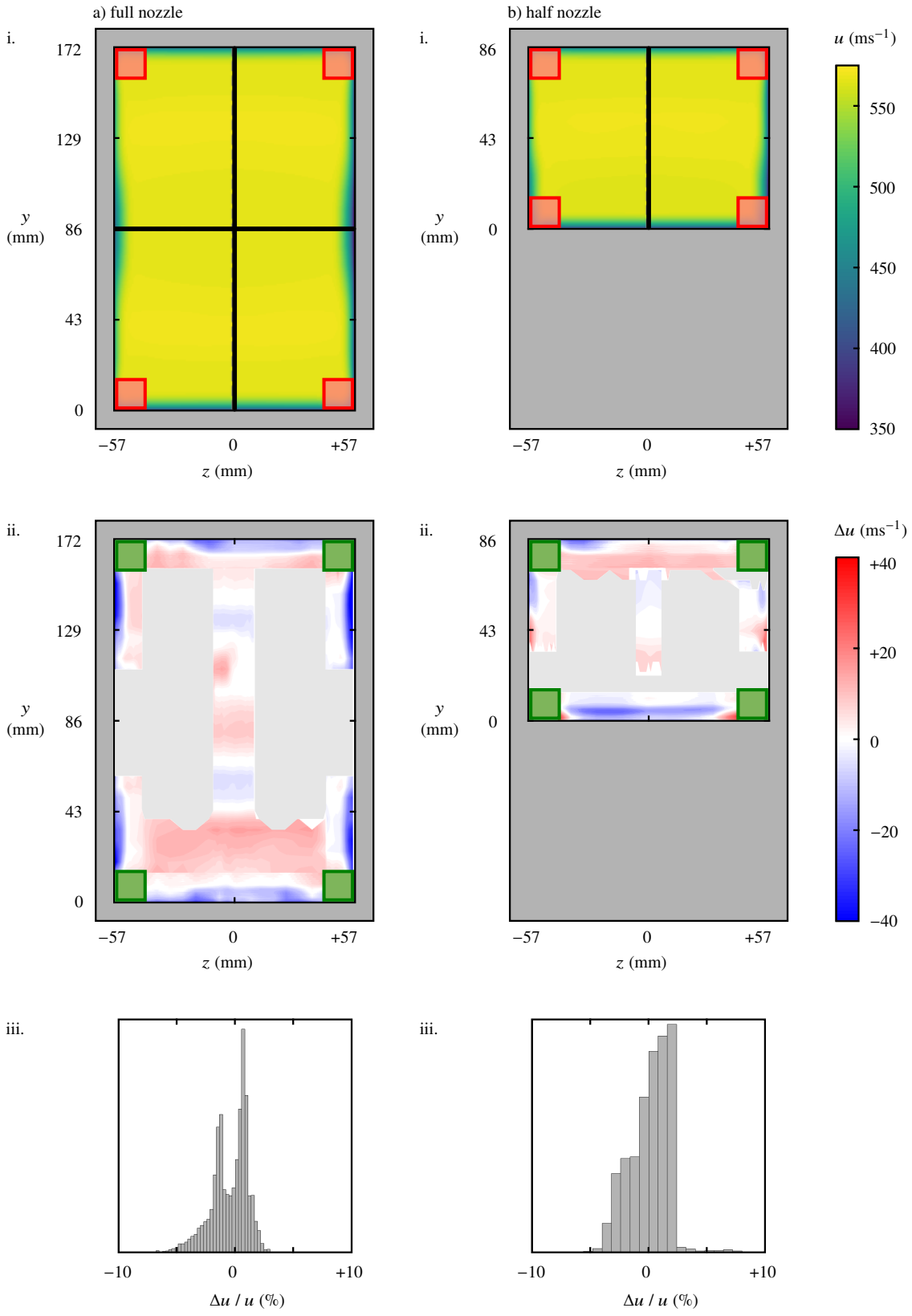

Fig. 11 Comparison between computations and experiment of the streamwise velocity at $x = 120$ mm for a) the full nozzle setup, and b) the half nozzle setup: i. the computed streamwise velocity; ii. difference between the computed velocity and equivalent experimental data (Fig. 5); iii. histogram of percentage velocity differences between computations and experiment.

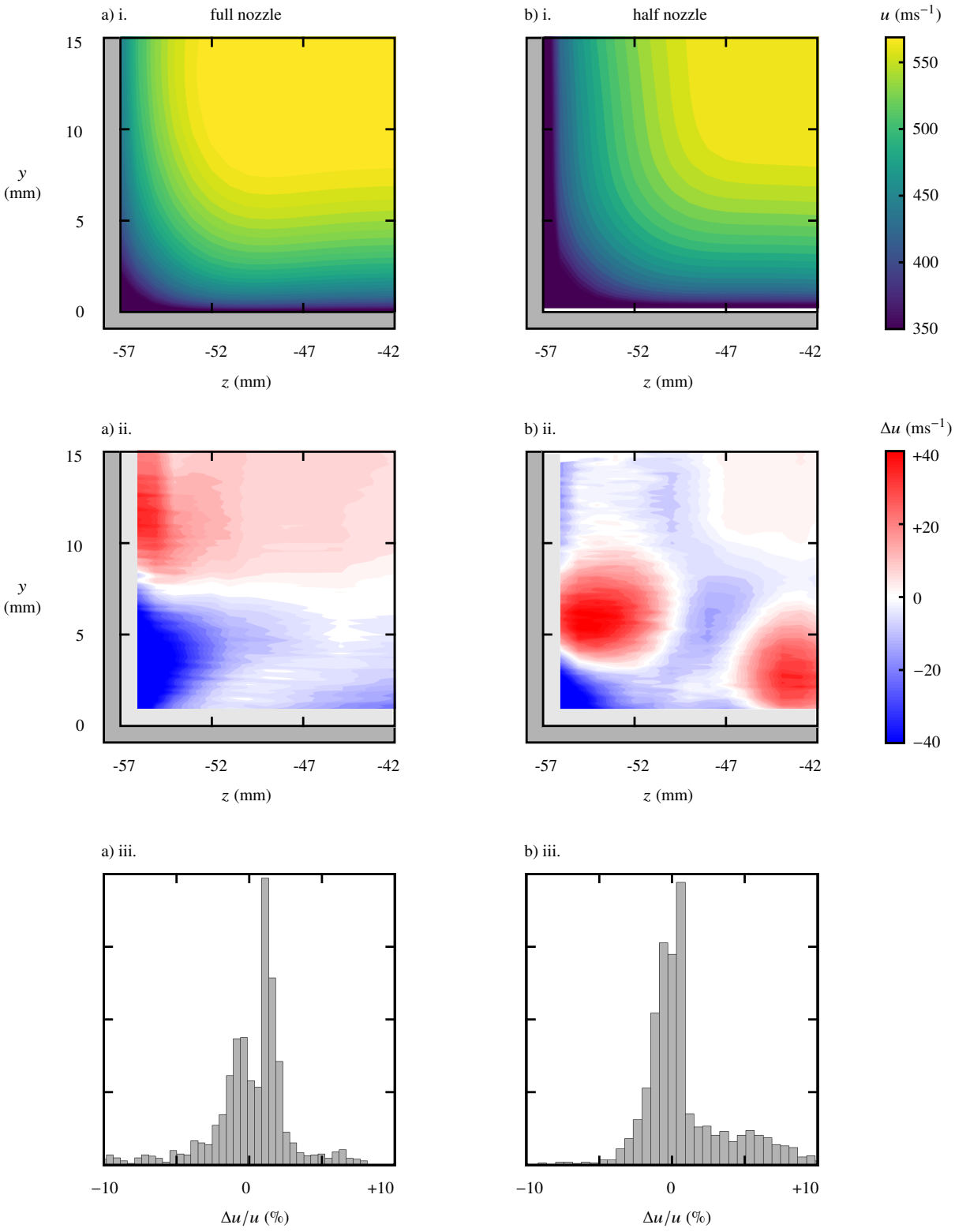

Fig. 12 Bottom corner regions for a) the full nozzle setup, and b) the half nozzle setup: i. streamwise velocity from computations using the Spalart–Allmaras model without the quadratic constitutive relation; ii. difference between streamwise velocity from computations and equivalent experimental data; iii. histogram of percentage differences in streamwise velocity between computations and experiment.

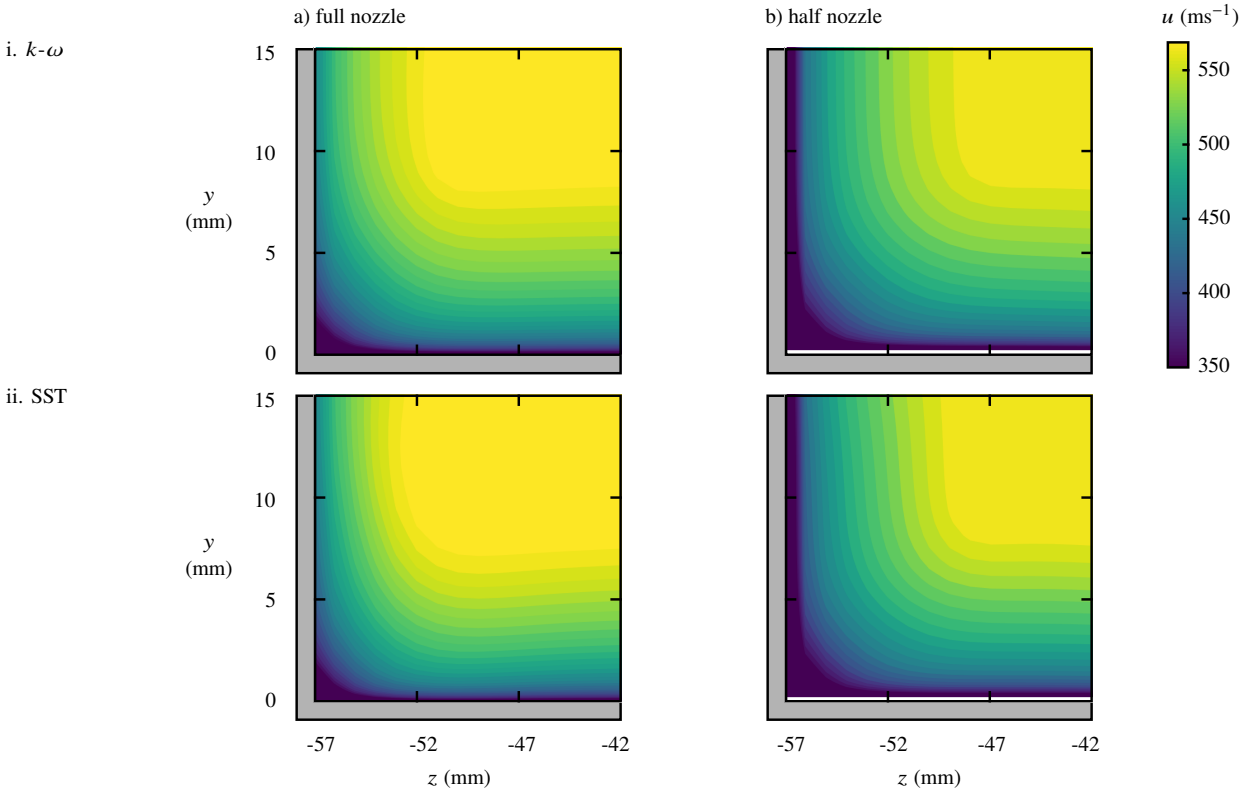

Fig. 13 Streamwise velocity in the bottom corner regions for a) the full nozzle setup, and b) the half nozzle setup: i. k-ω turbulence model; ii. SST turbulence model.

minimum error' during validation of the corner regions.

Therefore, whilst the precise wind tunnel flow might not be computed exactly, the simulations do appear to capture much of the key physics and can be used for validation purposes.

IV. Validation

The validation stage of the study is focused on the corner regions of the tunnel, marked in Fig. 2, which had been excluded in the previous section. The structure of the corner boundary layer is influenced by both the vorticity-generating Reynolds stress anisotropies and the secondary flows within the sidewall boundary layers. The secondary flows appear to be captured by the simulations (Fig. 11), which contain knowledge of the nozzle geometry. Therefore, these computations can be compared with the experimental data from Fig. 6 to validate the capabilities of different numerical models in corner flow prediction.

A. Linear eddy-viscosity turbulence models

The two distinct corner flow structures used for validation tests, are the bottom corners of the full nozzle and the half nozzle setups. In each case, the streamwise velocity in the 15 mm × 15 mm around the corner is extracted from the computations of the wind tunnel flow. This data is shown for the Spalart–Allmaras turbulence model in Fig. 12a-i for the full nozzle setup and in Fig. 12b-i for the half nozzle arrangement.

A comparison with the equivalent experimental data (Fig. 6) shows that the constituent floor and sidewall boundary-layer thicknesses are correctly determined by these computations. However, for both nozzle setups, the computations show a smooth transition between the sidewall and the floor boundary layers. This contrasts with the more complex shape of the corner boundary layer from experiment, which is believed to be perturbed by embedded vortices. Indeed, Figs. 12a-ii and 12b-ii show that the departures from the experimental velocities are as large as 40 ms^{-1}, or 7% of the freestream velocity. The spatial distribution of the velocity difference in these figures also displays clear structures,

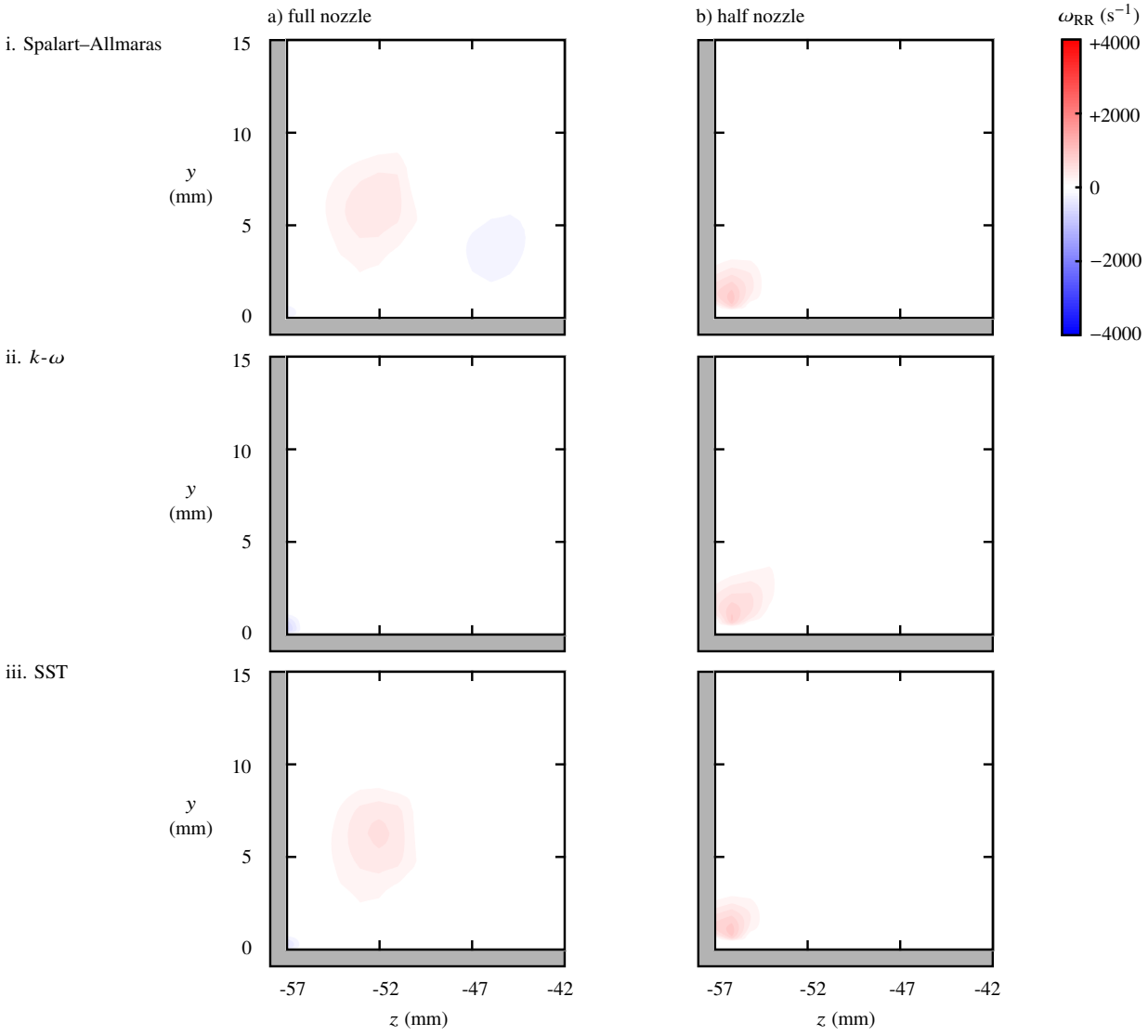

Fig. 14 Rigid-body component of streamwise vorticity in the bottom corner regions for a) the full nozzle setup, and b) the half nozzle setup: i. Spalart–Allmaras turbulence model; ii. k–ω turbulence model; iii. SST turbulence model.

Table 2 Percentage error in corner flow computations using different turbulence models for both nozzle setups when compared with experimental data from Fig. 6. These correspond to velocity distributions shown in Fig. 12 (Spalart–Allmaras) and in Fig. 13 (k–ω and SST).

turbulence model	percentage error	
	full nozzle	half nozzle
Spalart–Allmaras	6.74%	6.82%
k–ω	6.26%	7.52%
SST	6.02%	6.76%

which can perhaps be associated with vortices that exist in the physical flow but are missing from the computations. From the corresponding histograms in Figs. 12a-iii and 12b-iii, a typical error can be calculated, defined such that 95% of data points do not exceed this deviation from the velocity measurements. This error is determined to be 6.7% with the full nozzle (Fig. 12a-iii) and 6.8% with the half nozzle (Fig. 12b-iii), much larger than the discrepancies ($\approx 3\%$) estimated for the well-predicted regions of the flow field.

The streamwise velocity distribution of the k–ω and the SST turbulence models, which are also based on a linear eddy-viscosity hypothesis, are shown in Fig. 13. These computed flow fields are are almost identical to the Spalart–Allmaras model for both nozzle setups, exhibiting a smooth transition from the sidewall to the floor boundary layers. The discrepancy from experimental data, listed in Table 2, is in the range 6–8%, roughly the same for all three linear eddy-viscosity models investigated. This finding provides evidence that the poor prediction of corner flows is not specific to the Spalart–Allmaras model but is likely a feature of linear eddy-viscosity turbulence models in general.

In order to further investigate whether the error can be attributed to a lack of vortices in this region, the rigid-body component of streamwise vorticity, ω_{RR}, is extracted from the computations. This quantity, defined by Kolář, is calculated by removing the effects of mean shear and of irrotational strain from the vorticity field [29]. Figure 14 shows this vorticity distribution extracted from the simulations using the three turbulence models under consideration. In all three cases, the corner region contains no vorticity greater than 500 $\mathrm{s}^{-1} \approx 0.006\, u_\infty/\delta$, where u_∞ is the freestream velocity and δ is the nominal local boundary-layer thickness. It therefore appears that computations based on linear eddy-viscosity models are unable to generate the stress-induced corner vortices which exist in the physical flow.

B. The quadratic constitutive relation

Equivalent computations were also performed using the Spalart–Allmaras model with the QCR-2013 form of the quadratic constitutive relation [5]. The streamwise velocity distribution in the corner region, shown in Figs. 15a-i and 15b-i, suggests that the sidewall and floor boundary-layer thicknesses are still well-predicted. More importantly, the shape of the corner boundary layer now seems to better correspond to the measurements. Indeed, Figs. 15a-ii and 15b-ii suggest that the deviation from experimental values is reduced considerably, with velocity differences generally not exceeding 25 ms^{-1}. This discrepancy corresponds to 4.1% for the full nozzle setup (Fig. 15a-iii) and 5.6% for the half nozzle setup (Fig. 15b-iii).

The improvements in flow field prediction are thought to be due to the corner vortices being simulated more accurately when the quadratic constitutive relation is used. This is confirmed by the rigid-body component of vorticity within the corner region, shown in Fig. 16. In contrast to Fig. 14, there are now obvious vortices within the corner boundary layer. Note that in Fig. 16a, the full nozzle setup shows a floor vortex close to the corner, and a sidewall vortex displaced upwards away from the corner. This is consistent with the measured vorticity distribution from Fig. 6a. Similarly, the configuration of vortices with the half nozzle (Fig. 16b) agrees well with the asymmetric vortex pair structure suggested in Fig. 6b.

C. Effect of changing the QCR constant

The computations with QCR in the preceding section use the recommended value of the constant, $c_{cr1} = 0.3$, which was calibrated in the outer part of an equilibrium turbulent boundary layer [5]. However, in practice, this 'constant' is generally used as a tuning parameter. Computations with different values of c_{cr1} were therefore investigated.

The streamwise velocity distribution in the bottom corner region is presented in Fig. 12 for $c_{cr1} = 0$ and in Fig. 15 for $c_{cr1} = 0.3$. Equivalent velocity distributions with $c_{cr1} = 0.1$, 0.2, 0.4, and 0.5 are given for the full nozzle and the

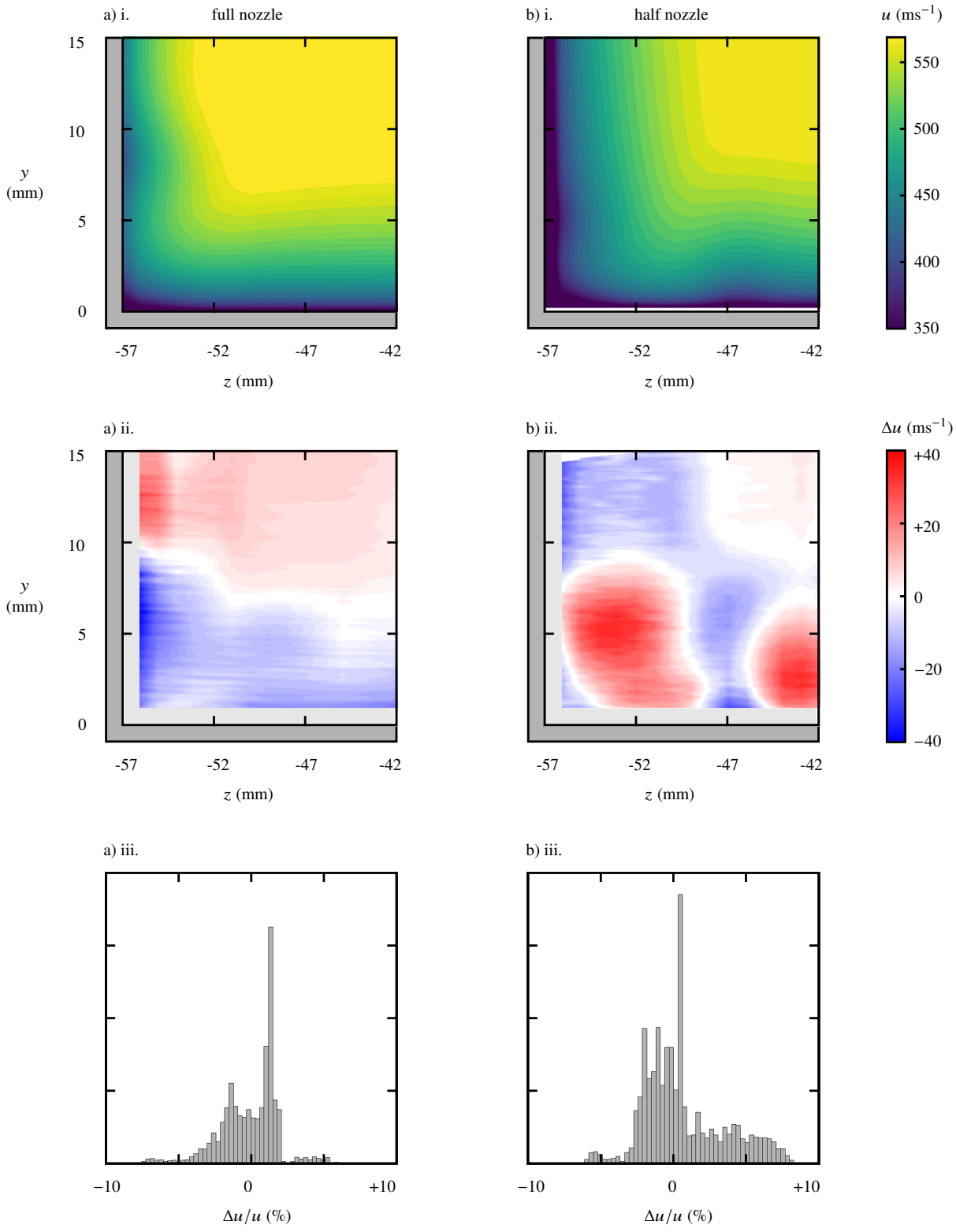

Fig. 15 Bottom corner regions for a) the full nozzle setup, and b) the half nozzle setup: i. streamwise velocity from computations using the Spalart–Allmaras model with QCR-2013; ii. difference between streamwise velocity from computations and equivalent experimental data; iii. histogram of percentage differences in streamwise velocity between computations and experiment.

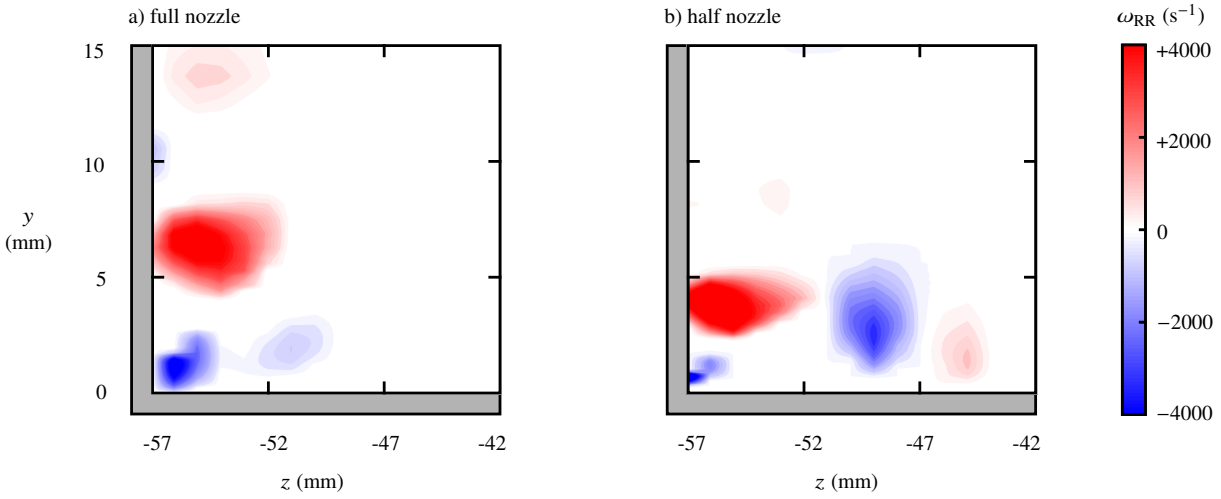

Fig. 16 The rigid-body component of streamwise vorticity, ω_{RR}, in the bottom corner region from computations using the Spalart–Allmaras model with QCR-2013 for a) the full nozzle setup, and b) the half nozzle setup.

Table 3 Spatial correlation coefficient, $\tilde{C}$, calculated for the velocity data presented in Figs. 12, 15 and 17.

c_{cr1}	$\tilde{C}$	
	full nozzle	half nozzle
0 (no QCR)	0.936	0.969
0.1	0.948	0.975
0.2	0.962	0.978
0.3 (default value)	0.975	0.977
0.4	0.981	0.970
0.5	0.979	0.962

half nozzle setups in Figs. 17a and 17b, respectively. The corner boundary layer shape shows increasing distortion as the value of c_{cr1} is increased.

In order to assess how well these computations match the experimental data (Fig. 6), a typical error is calculated for each case, defined such that 95% of data points do not exceed this deviation from the experimentally-determined velocities. Figure 18 plots this error as a function of c_{cr1} for both nozzle setups. In both cases, as c_{cr1} increases, the error initially gets smaller before reaching a minimum and increasing again. The minimum error occurs at $c_{cr1} = 0.4$ for the full nozzle and at $c_{cr1} = 0.2$ for the half nozzle. In both these cases, the recommended c_{cr1} value of 0.3 does not produce the best fit to experimental data but, when the error is averaged over the two nozzle setups, the minimum does indeed lie at $c_{cr1} = 0.3$. This finding therefore supports the use of the recommended value of the QCR constant in computing such supersonic corner flows.

It is important to note, however, that this finding relates specifically to the corner boundary layers of supersonic channel flows measured in the current study, and so the behaviour of coefficients is valid only for this flow field. Therefore, the results of this analysis should not be used directly to choose QCR coefficients in computations of any other types of flow. In addition, the error metric used for the current analysis (defined such that 95% of data points lie within this deviation from the measured velocity) is only one possible measure of the agreement between experimental and computational data. This method of estimating error is particularly useful because it can be directly compared to the 'minimum expected error' determined in Section III.B. However, another insightful metric is the spatial correlation coefficient:

$$\tilde{C} = \frac{\left\langle u_{\mathrm{exp}}\, u_{\mathrm{comp}} \right\rangle - \left\langle u_{\mathrm{exp}} \right\rangle \left\langle u_{\mathrm{comp}} \right\rangle}{\left[\left(\left\langle u_{\mathrm{exp}}^2 \right\rangle - \left\langle u_{\mathrm{exp}} \right\rangle^2 \right) \left(\left\langle u_{\mathrm{comp}}^2 \right\rangle - \left\langle u_{\mathrm{comp}} \right\rangle^2 \right) \right]^{1/2}}, \tag{6}$$

where u_{exp} and u_{comp} represent the experimental and computational streamwise velocity data, respectively, and the

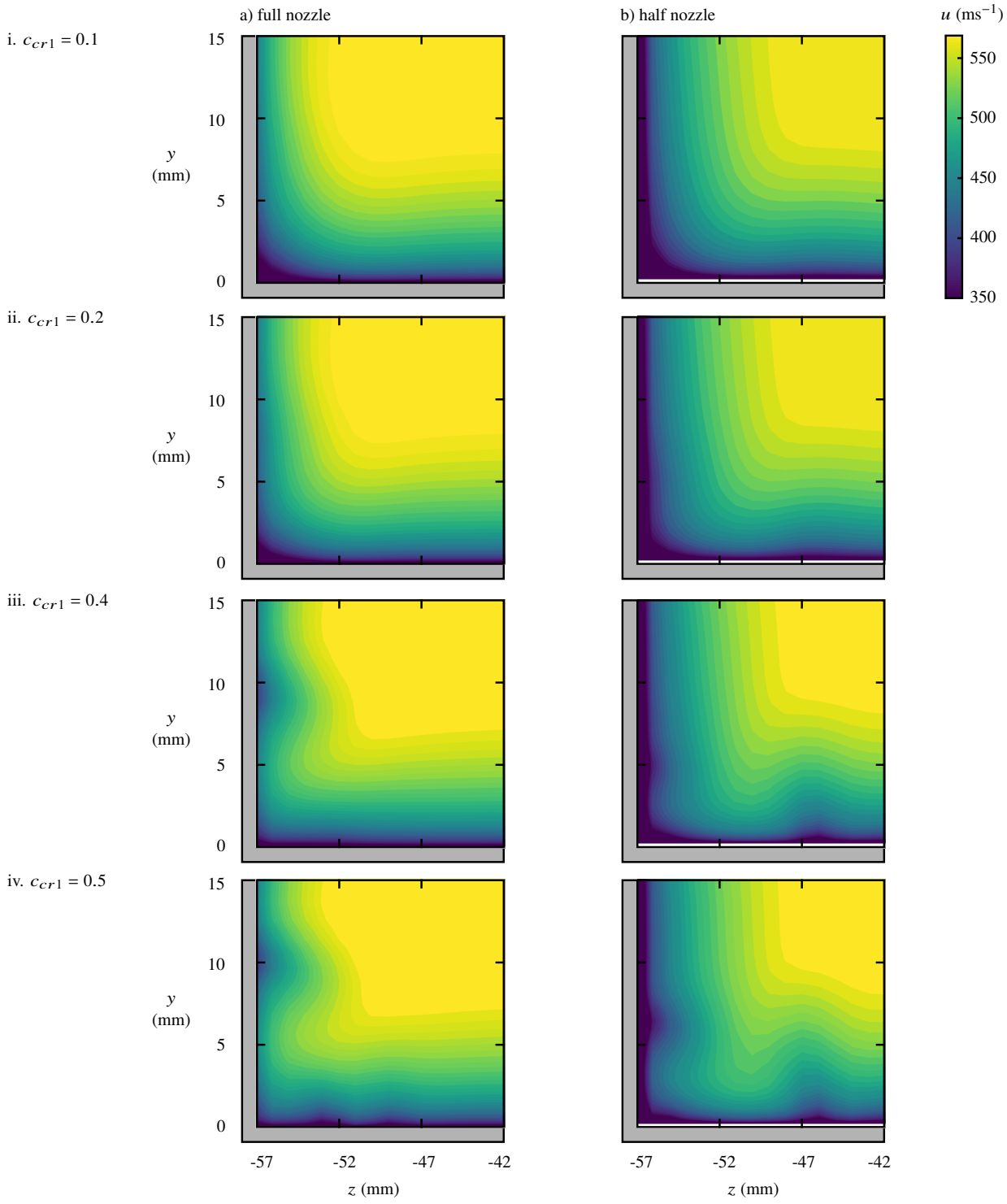

Fig. 17 Effect of varying c_{cr1} on the streamwise velocity in the bottom corner regions for a) the full nozzle setup, and b) the half nozzle setup: i. c_{cr1} = 0.1; ii. c_{cr1} = 0.2; iii. c_{cr1} = 0.4; iv. c_{cr1} = 0.5.

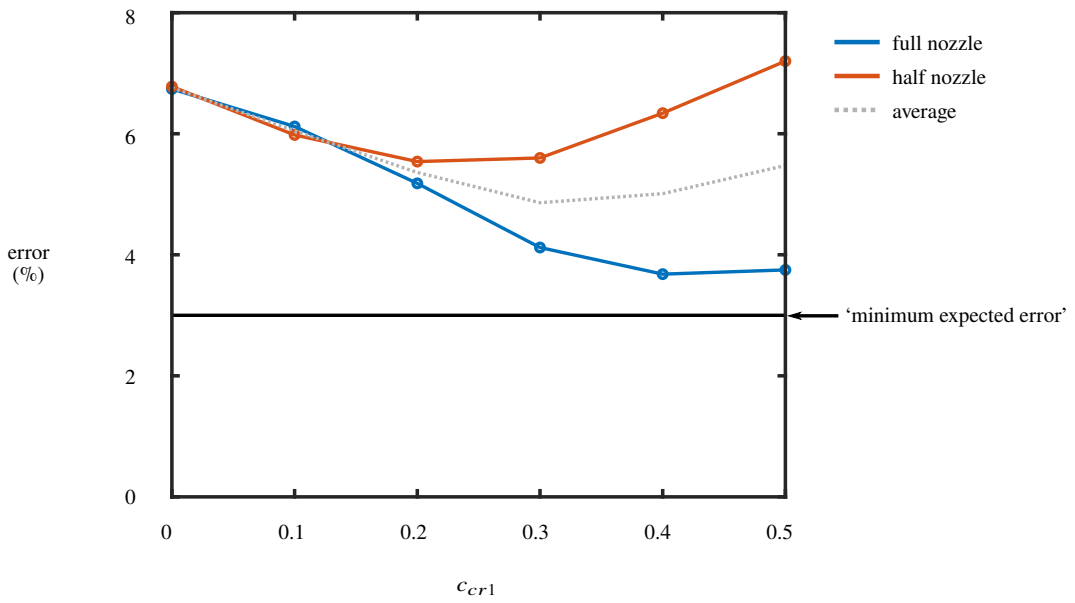

Fig. 18 Typical error between computations and experimental data as a function of c_{cr1} for both nozzle setups. The minimum expected error is determined from velocity errors between experiment and computation in the wider flow field (Fig. 11).

angled brackets denote a spatial average over the validation region. The correlation coefficient takes values from -1 to 1 by construction, with $\tilde{C} = 0$ corresponding to no correlation and $\tilde{C} = 1$ indicative of perfect agreement between computation and experiment. The calculated values of $\tilde{C}$ for each computational case are listed in Table 3. These coefficients highlight the subtle nature of the effect of QCR but show the same broad trends as the error metric from Fig. 18, with maximum correlation observed at $c_{cr1} = 0.4$ for the full nozzle and at $c_{cr1} = 0.2$ for the half nozzle.

Whatever the choice of error metric, it is useful to investigate the topology of streamwise corner vortices in order to better understand the shape of the error curves in Fig. 18 . For each case from Fig. 17, the distribution of the rigid-body component of streamwise vorticity is plotted in Fig. 19. Here, the strength of the counter-rotating vortex pair is seen to initially strengthen as c_{cr1} is increased. As the strength of these vortices approaches those in the physical flow, the corner boundary-layer shape is better predicted and the difference between computation and experiment is reduced, as seen in Fig. 18.

However, when c_{cr1} reaches approximately 0.5 for the full nozzle and 0.3 for the half nozzle, the appearance of additional vortices can be observed. Such vortices, thought to be non-physical, have been reported in similar computations at high values of c_{cr1} by Leger *et al.* [8]. These spurious vortices modify the shape of the corner boundary layer in a manner which does not reflect the true flow. As a result, the calculated error in Fig. 18 for both setups is seen to increase for c_{cr1} large enough that the additional vortices are produced.

V. Conclusions

Despite the importance of the boundary layers along streamwise corner geometries in supersonic flow, these regions are generally not predicted reliably by RANS methods typically used in industry. This paper uses experimental velocity data obtained in the corner regions of a Mach 2.5 wind tunnel flow to validate a range of numerical approaches. The RANS computations used for this process are carefully set up using a range of detailed characterisation data to ensure that they are representative of the physical wind tunnel flow. An evaluation of the overall, relatively well-predicted flow field suggests a minimum expected error of approximately 3% for the validation process.

Three popular turbulence models — Spalart–Allmaras, Menter SST, and Wilcox k–ω — are found not to accurately represent the measured corner flow. The complex boundary-layer edge structure is not reproduced by these computations, resulting in velocity differences up to 7%. These errors can be attributed to the reliance of these turbulence models on the linear eddy-viscosity assumption, resulting in an inability to generate the stress-induced corner vortices which

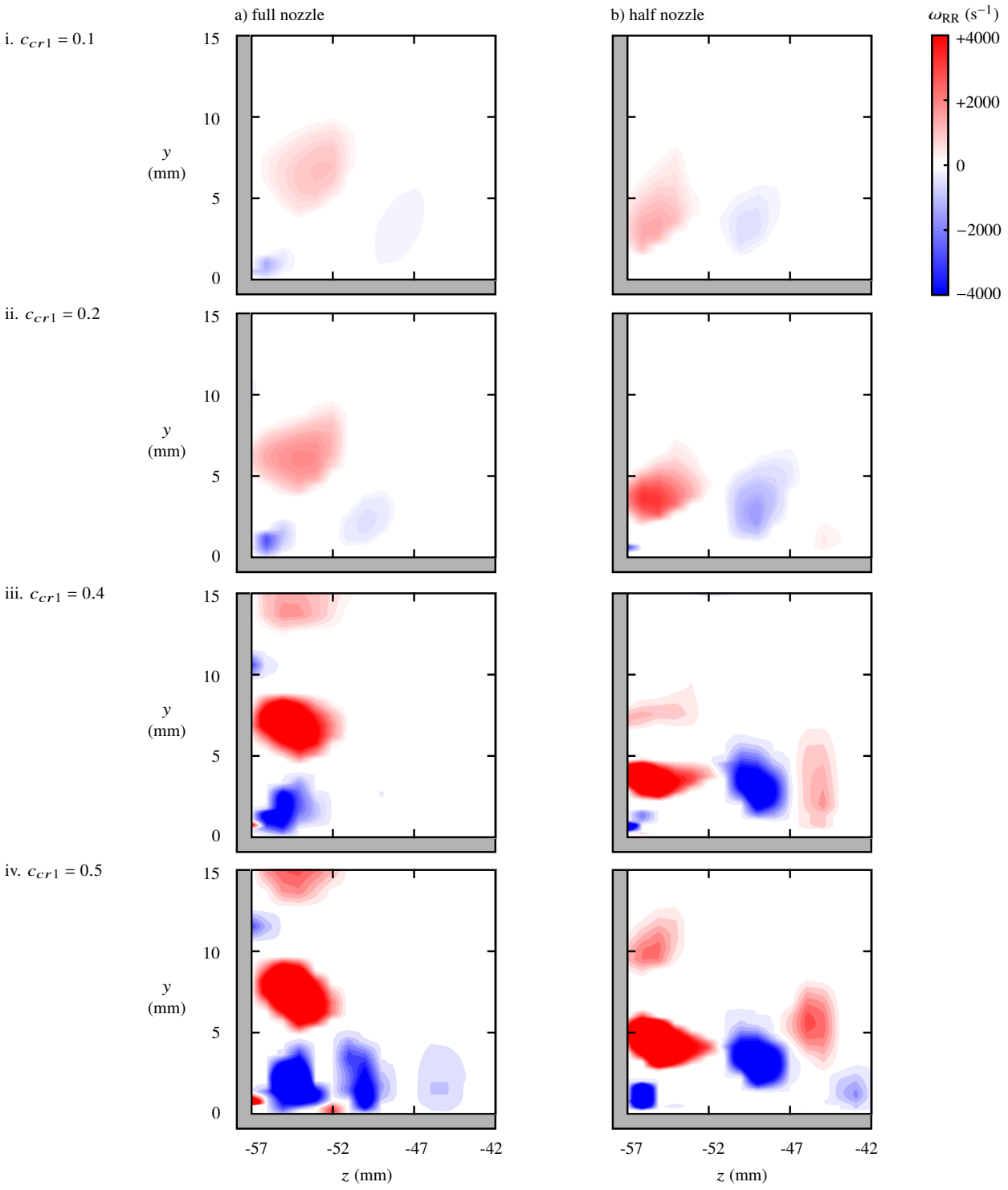

Fig. 19 Effect of varying c_{cr1} on the rigid-body component of streamwise vorticity in the bottom corner regions for a) the full nozzle setup, and b) the half nozzle setup: i. c_{cr1} = 0.1; ii. c_{cr1} = 0.2; iii. c_{cr1} = 0.4; iv. c_{cr1} = 0.5.

modify the local flow.

When the quadratic constitutive relation is introduced, the vortices and, in turn, flow structure in the corner regions are better predicted. The discrepancy from experimental velocity data is reduced to about 4–5%, much closer to the minimum expected 3% error. However, the measured boundary-layer structure is not exactly captured by these simulations which implies that, whilst vortices are generated, their strength and position appear to differ somewhat from the physical corner vortices. Moreover, when the value of the coefficient c_{cr1}, often treated as a tuning parameter, exceeds the recommended value of 0.3, additional non-physical vortices are generated which cause increased deviation from experimental data.

Therefore, through generating corner vortices, QCR has been shown to increase the accuracy of corner flow computations, providing evidence to support its use where such flows are likely to be important. These findings explain why the prediction of corner separation is improved when QCR is used. The results from such computations should, however, be treated with some degree of caution since the position and strength of the generated vortices do not exactly match those in physical flows. Furthermore, the value of c_{cr1} should not exceed 0.3 without ensuring that spurious vortices have not been produced through careful analysis of the computed flow field.

Acknowledgements

This material is based upon work supported by the US Air Force Office of Scientific Research under award number FA9550–16–1–0430. The authors would like to thank David Martin, Sam Flint, Anthony Luckett and Ciaran Costello for operating the blowdown wind tunnel. The wind tunnel is part of the UK National Wind Tunnel Facility (NWTF) and their support is gratefully acknowledged.

References

[1] Benek, J., "Corner flows: Motivation and objectives," 2017. Comments made at the *10th Annual Shock Wave/Boundary Layer Interaction (SWBLI) Technical Interchange Meeting*.

[2] Gessner, F., "The origin of secondary flow in turbulent flow along a corner," *Journal of Fluid Mechanics*, Vol. 58, No. 1, 1973, pp. 1–25.

[3] Gessner, F., and Jones, J., "On some aspects of fully-developed turbulent flow in rectangular channels," *Journal of Fluid Mechanics*, Vol. 23, No. 4, 1965, pp. 689–713.

[4] Spalart, P., "Strategies for turbulence modelling and simulations," *International Journal of Heat and Fluid Flow*, Vol. 21, No. 3, 2000, pp. 252–263.

[5] Mani, M., Babcock, D., Winkler, C., and Spalart, P., "Predictions of a supersonic turbulent flow in a square duct," *51st AIAA Aerospace Sciences Meeting*, 2013-0860.

[6] Rumsey, C., Carlson, J., Pulliam, T., and Spalart, P., "Improvements to the quadratic constitutive relation based on NASA Juncture Flow data," *AIAA Journal*, 2020. Submitted.

[7] Dandois, J., "Improvement of corner flow prediction using the quadratic constitutive relation," *AIAA Journal*, Vol. 52, No. 12, 2014, pp. 2795–2806.

[8] Leger, T., Bisek, N., and Poggie, J., "Supersonic corner flow predictions using the quadratic constitutive relation," *22nd AIAA Computational Fluid Dynamics Conference*, 2015-3432.

[9] Bisek, N., "High-fidelity simulations of the UTSI Mach 2 test section," *2018 AIAA Aerospace Sciences Meeting*, 2018-1097.

[10] Rumsey, C., Carlson, J., and Ahmad, N., "FUN3D Juncture Flow computations compared with experimental data," *AIAA Scitech 2019 Forum*, 2019-0079.

[11] Colliss, S., "Vortical structures on three-dimensional shock control bumps," Ph.D. thesis, University of Cambridge, 2014.

[12] Sun, C., and Childs, M., "A modified wall wake velocity profile for turbulent compressible boundary layers." *Journal of Aircraft*, Vol. 10, No. 6, 1973, pp. 381–383.

[13] Musker, A., "Explicit expression for the smooth wall velocity distribution in a turbulent boundary layer," *AIAA Journal*, Vol. 17, No. 6, 1979, pp. 655–657.

[14] Titchener, N., Colliss, S., and Babinsky, H., "On the calculation of boundary-layer parameters from discrete data," *Experiments in Fluids*, Vol. 56, No. 8, 2015, p. 159.

[15] Sabnis, K., and Babinsky, H., "Nozzle geometry effects on corner boundary layers in supersonic wind tunnels," *AIAA Journal*, Vol. 57, No. 8, 2019, pp. 3620–3623.

[16] Sabnis, K., Babinsky, H., Galbraith, D., and Benek, J., "Flow characterisation for a validation study in high-speed aerodynamics," *2019 Fluid Dynamics Conference*, 2019-3073.

[17] Benek, J., Steger, J., and Dougherty, F., "A flexible grid embedding technique with application to the Euler equations," *6th Computational Fluid Dynamics Conference*, 1983-1944.

[18] "Pointwise Version 18.0R4," *Pointwise Incorporated*, 2017.

[19] Buning, P., et al., "Overflow user's manual," Tech. rep., NASA Langley Research Center, 2002.

[20] Toro, E., Spruce, M., and Speares, W., "Restoration of the contact surface in the HLL–Riemann solver," *Shock Waves*, Vol. 4, No. 1, 1994, pp. 25–34.

[21] Koren, B., "Upwind schemes, multigrid and defect correction for the steady Navier–Stokes equations," *11th International Conference on Numerical Methods in Fluid Dynamics*, Springer, 1989, pp. 344–348.

[22] Tramel, R., and Nichols, R., "A highly efficient numerical method for overset-mesh moving-body problems," *13th Computational Fluid Dynamics Conference*, 1997-2040.

[23] Spalart, P., and Allmaras, S., "A one-equation turbulence model for aerodynamic flows," *30th Aerospace Sciences Meeting and Exhibit*, 1992-0439.

[24] Allmaras, S., and Johnson, F., "Modifications and clarifications for the implementation of the Spalart–Allmaras turbulence model," *Seventh International Conference on Computational Fluid Dynamics*, ICCFD7-1902, 2012.

[25] Menter, F., and Rumsey, C., "Assessment of two-equation turbulence models for transonic flows," *Fluid Dynamics Conference*, 1994-2343.

[26] Menter, F., Kuntz, M., and Langtry, R., "Ten years of industrial experience with the SST turbulence model," *Turbulence, Heat and Mass Transfer*, Vol. 4, No. 1, 2003, pp. 625–632.

[27] Wilcox, D., "Reassessment of the scale-determining equation for advanced turbulence models," *AIAA Journal*, Vol. 26, No. 11, 1988, pp. 1299–1310.

[28] Wilcox, D., *Turbulence Modeling for CFD*, 3rd ed., DCW Industries Incorporated, 2006.

[29] Kolář, V., "Vortex identification: New requirements and limitations," *International Journal of Heat and Fluid Flow*, Vol. 28, No. 4, 2007, pp. 638–652.